

Analysis of the signal measured in spectral-domain optical coherence tomography based on nonlinear interferometers

Arturo Rojas-Santana 

Tecnologico de Monterrey, School of Engineering and Science, Avenida Eugenio Garza Sada 2501, Monterrey, Nuevo León 64849, Mexico

Gerard J. Machado 

ICFO–Institut de Ciències Fòniques, The Barcelona Institute of Science and Technology, 08860 Castelldefels, Barcelona, Spain

Maria V. Chekhova 

*Max-Planck Institute for the Science of Light, Staudtstraße 2, Erlangen 91058, Germany
and Friedrich-Alexander University of Erlangen-Nuremberg, Staudtstraße 7/B2, Erlangen 91058, Germany*

Dorilian Lopez-Mago *

Tecnologico de Monterrey, School of Engineering and Science, Avenida Eugenio Garza Sada 2501, Monterrey, Nuevo León 64849, Mexico

Juan P. Torres †

*ICFO–Institut de Ciències Fòniques, The Barcelona Institute of Science and Technology, 08860 Castelldefels, Barcelona, Spain
and Departament of Signal Theory and Communications, Universitat Politècnica de Catalunya, 08034 Barcelona, Spain*



(Received 21 January 2022; accepted 26 August 2022; published 6 September 2022)

We analyze and compare the output signals obtained in three different configurations of optical coherence tomography (OCT). After appropriate processing, these signals are used to retrieve an image of the sample under investigation. One of the configurations considered is the common choice in most OCT applications and is based on the use of a Michelson interferometer. For brevity, here we refer to it as standard OCT. The other two configurations are two types of optical coherence tomography based on the use of so-called nonlinear interferometers, interferometers that contain optical parametric amplifiers inside. The goal is to highlight the differences and similarities between the output signals measured in standard OCT and in these two OCT schemes, with the aim of evaluating if retrieval of information about the sample can be better done in one case over the others. We consider schemes where the optical sectioning of the sample is obtained by measuring the output signal spectrum (spectral or Fourier-domain OCT), since it shows better performance in terms of speed and sensitivity than the counterpart time-domain OCT.

DOI: [10.1103/PhysRevA.106.033702](https://doi.org/10.1103/PhysRevA.106.033702)

I. INTRODUCTION

Optical coherence tomography (OCT) is a three-dimensional high-resolution imaging scheme that produces tomographic images of a variety of objects, such as biological systems, by measuring light backscattered from the samples [1]. In order to obtain good transverse resolution (in the plane perpendicular to the beam propagation axis), OCT focuses light into a small spot that is scanned over the sample. To obtain good resolution in the axial direction (optical sectioning along the beam propagation direction), OCT uses light with a large bandwidth. Optical coherence tomography is a highly mature optical imaging technology as well as a very active topic of research (see, for instance, [2] for reports on advances in optical coherence tomography).

The first OCT systems were put forward and demonstrated in [3,4] and most of the current OCT systems follow the same general structure of these pioneering experiments. They use a broadband light beam that splits into two beams in a Michelson interferometric setup: the reference and object beams. The output signal results from the combination of the reference beam with the object beam after being reflected from the sample. We will refer to these OCT systems as standard OCT, although we should remark that there is still a rich variety among these conventional OCT systems.

In the past few years several research groups have demonstrated new OCT schemes based on nonlinear interferometers [5–8] and interferometers that contain parametric amplifiers [9]. The main advantage of these quantum schemes is that they allow probing the sample at a chosen wavelength, for instance, in the far infrared, to achieve higher penetration depth into the sample, while at the same time using an optimum wavelength for efficient detection. Nonlinear interferometers are key elements in numerous applications, namely, in imaging [10,11], sensing [12], spectroscopy [13–15], and microscopy [16,17].

*dlopezmago@tec.mx

†juanp.torres@icfo.eu

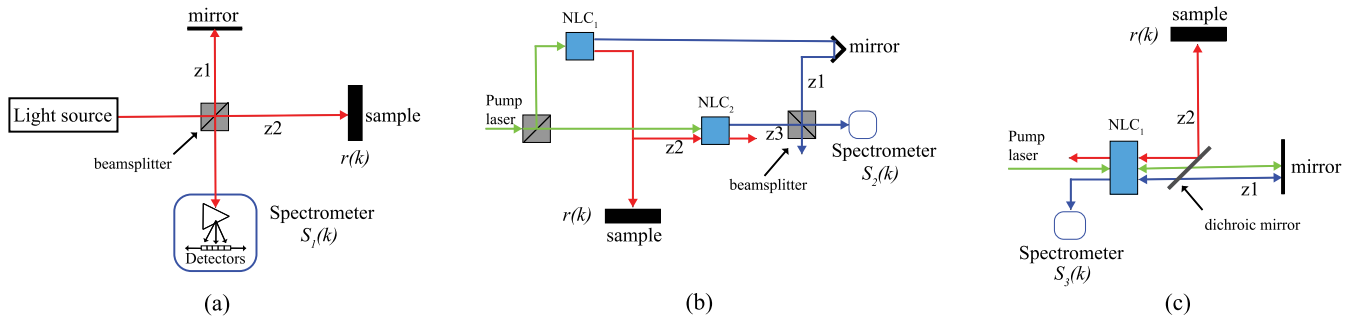


FIG. 1. Sketch of the three OCT configurations considered: (a) standard FD-OCT, (b) FD-OCT based on induced coherence, and (c) FD-OCT based on an SU(1,1) interferometer. Here $S_i(k)$ ($i = 1, 2, 3$) are the spectral densities measured for each configuration, which are labeled with different subscripts for the sake of clarity; $r(k)$ is the reflection coefficient of the sample, which depends on its internal layer structure; and z_1 , z_2 , and z_3 are optical paths taken by light beams. Different colors depict light beams (photons) at different central wavelengths. In (b) and (c), NLC refers to nonlinear crystal.

There are two general configurations considered. One scheme is based on the concept of induced coherence [18–20]; the other scheme is an SU(1,1) interferometer [21]. We will analyze the OCT signal obtained in both configurations. For the sake of comparison, we will also consider the signal obtained in a standard OCT scheme.

There are two procedures to obtain the internal axial structure of samples (optical sectioning) in OCT. In time-domain OCT (TD-OCT), each axial scan of the sample consists of the signal measured for an array of different delays introduced in the reference arm of the interferometer. For each delay, the intensity of the signal resulting from the combination of the reference and object beams is measured. The internal structure of the sample is reconstructed from the interferogram obtained plotting the signal measured versus delays. In spectral or Fourier-domain OCT (FD-OCT) [22] (see also Chap. 5 in Ref. [1]) one retrieves the structure of the sample along the axial direction by Fourier transforming the spectrum of the interferogram with a fixed delay in the reference arm. FD-OCT avoids the need of TD-OCT for displacing mechanically a mirror and consequently is more robust and allows faster data acquisition. Moreover, it shows better sensitivity than TD-OCT [23]. Here we will restrict ourselves to the analysis of OCT signal obtained in FD-OCT in all cases considered.

We will show (see Secs. III and IV) that the signal measured in the FD-OCT scheme based on nonlinear interferometers shows a fundamental and advantageous difference when compared with the signal measured in standard OCT. In standard OCT peaks appear in the output signal whose location does not depend on the optical path imbalance of the interferometer, the so-called autocorrelation terms. In certain regimes, these terms are not present in the OCT schemes based on nonlinear interferometers considered here. These autocorrelation terms appear as artifacts in typical OCT schemes and should be suppressed when possible [1].

We will also show (see Sec. IV) that the signal measured in the FD-OCT scheme based on an SU(1,1) nonlinear interferometer is larger than the signal that probes the sample. This might be important to probe highly sensitive samples, since it allows one to probe the sample with a low-photon flux while detecting a high-photon flux signal at the detection

stage, which might make easier the election of the detection system.

Finally, the observation that certain features of the OCT signals in nonlinear interferometers are also present in standard OCT might benefit the new schemes since they can profit from the wealth of research and technology related to conventional OCT systems. This is the case of the sensitivity decay observed in all systems that make use of FD-OCT (see Sec. V). We show that the same techniques applied in standard OCT to correct this effect can also be used in OCT schemes based on nonlinear interferometers.

II. STANDARD FOURIER-DOMAIN OPTICAL COHERENCE TOMOGRAPHY

For the sake of comparison, we begin by describing a standard OCT configuration [see Fig. 1(a)], which will constitute the benchmark for all nonclassical OCT schemes (see, for instance, [1] for an excellent description of OCT and a detailed mathematical derivation of main equations). The sample of reference used in the calculations is a single layer with low reflectivity at both faces. Its reflectivity $r(k)$ with respect to the field can thus be written as

$$r(k) = r_1 + r_2 \exp(2ik_0 n_0 d + 2ikn_g d), \quad (1)$$

where $R_1 = |r_1|^2$ and $R_2 = |r_2|^2$ are the reflectivities of the first and second faces, n_0 is the refractive index at the central frequency, n_g is the group index, d is the sample thickness, $k = \Omega/c$ is the wave-number deviation from the central wave number $k_0 = \omega_0/c$, and Ω is the angular frequency deviation from the central frequency ω_0 .

FD-OCT uses light with a large bandwidth: The coherence length, which determines the axial resolution of OCT, is inversely proportional to the spectral bandwidth. We characterize the spectral density of the light source with a Gaussian function

$$\Phi(k) = \frac{1}{\pi^{1/2} W} \exp\left(-\frac{k^2}{W^2}\right), \quad (2)$$

The function $\Phi(k)$ is normalized so that $\int dk \Phi(k) = 1$. The FWHM spectral bandwidth of the laser source $\Delta\lambda$ is related to the parameter W as $\Delta\lambda = (\lambda_0^2 \sqrt{\ln 2/\pi}) W$, with λ_0 the central wavelength of the laser source. For the sake of simplicity,

throughout this paper we consider as the main variable the wave number, since the axial structure of samples is obtained from Fourier transforming the output signal written with k as variable.

Light is divided by a beam splitter into the reference and object beams in a Michelson interferometer. We consider a 50:50 beam splitter with reflection and transmission coefficients $1/\sqrt{2}$ and $i/\sqrt{2}$, respectively. The distance traversed by the reference beam is denoted by $2z_1$ and the distance traversed by the object beam is $2z_2 = 2(z_1 + s)$. Thus $2s$ is the optical path imbalance between the reference and object paths in the Michelson interferometer. The beams finally recombine at the beam splitter and a spectrometer measures the spectral density $S_1(k)$ of the output beam, which is given by

$$S_1(k) = \frac{\Phi(k)}{4} |\exp[2i(k_0 + k)z_1] + r(k) \exp[2i(k_0 + k)z_2]|^2. \quad (3)$$

This is the general expression of the spectral density of the OCT signal for an arbitrary reflection coefficient. After expanding the modulus in Eq. (3), the terms independent of s are the autocorrelation terms [1], while the two s -dependent terms are the cross-correlation terms. For the sample described by Eq. (1), the spectral density is

$$S_1(k) = \frac{1 + R_1 + R_2}{4} \Phi(k) + \frac{2(R_1 R_2)^{1/2}}{1 + R_1 + R_2} \Phi(k) \cos(2n_g d k + \varphi_1) + \frac{2R_1^{1/2}}{1 + R_1 + R_2} \Phi(k) \cos(2s k + \varphi_2) + \frac{2R_2^{1/2}}{1 + R_1 + R_2} \Phi(k) \cos(2s k + 2n_g d k + \varphi_3), \quad (4)$$

where $\varphi_1 = 2k_0 n_0 d$, $\varphi_2 = 2k_0 s$, and $\varphi_3 = 2k_0 (s + n_0 d)$.

In order to retrieve information about the sample, e.g., the location of the interfaces and reflection coefficients, we obtain the Fourier transform of the spectral density measured $S_1(k)$, i.e., $\tilde{S}_1(z) = \mathcal{F}[S_1(k)] = 1/(2\pi)^{1/2} \int dk S(k) \exp(-ikz)$. We find that

$$\tilde{S}_1(z) = \frac{1 + R_1 + R_2}{4} \tilde{\Phi}(z) + \frac{(R_1 R_2)^{1/2}}{4} [\tilde{\Phi}(z - 2n_g d) \exp(i\varphi_1) + \tilde{\Phi}(z + 2n_g d) \exp(-i\varphi_1)] + \frac{R_1^{1/2}}{4} [\tilde{\Phi}(z - 2s) \exp(i\varphi_2) + \tilde{\Phi}(z + 2s) \exp(-i\varphi_2)] + \frac{R_2^{1/2}}{4} [\tilde{\Phi}(z - 2s - 2n_g d) \exp(i\varphi_3) + \tilde{\Phi}(z + 2s + 2n_g d) \exp(-i\varphi_3)], \quad (5)$$

where $\tilde{\Phi}(z) = \mathcal{F}[\Phi(k)]$ designates the Fourier transform.

In order to clearly identify the location and height of the peaks corresponding to the cross-correlation terms, it is important to have a sufficiently large value of the path-length difference s . If we define Δz_1 as the width of the function

$\tilde{\Phi}(z)$, which determines the axial resolution of OCT, an unequivocal identification of the characteristics of the sample requires $2s \gg \Delta z_1$, $2s + 2n_g d \gg \Delta z_1$, and $2n_g d \gg \Delta z_1$. In this case the typical shape of $\tilde{S}_1(z)$ contains seven characteristic peaks: a central peak at $z = 0$, three peaks located at $z > 0$, and another three peaks at $z < 0$. The peaks at $z \neq 0$ are located symmetrically around $z = 0$. The separation between the two cross-correlation peaks at $z > 0$ (or $z < 0$) is $2n_g d$, twice the optical thickness of the sample. For low reflectivity $R_{1,2} \ll 1$, the heights of the cross-correlation terms in comparison with the height of the peak at $z = 0$ are $R_1^{1/2}$ and $R_2^{1/2}$.

III. FOURIER-DOMAIN OPTICAL COHERENCE TOMOGRAPHY IN AN INDUCED COHERENCE CONFIGURATION

Figure 1(b) shows a sketch of an OCT scheme based on the concept of induced coherence [5]. Signal (s_1) and idler (i_1) photons are generated in the first nonlinear crystal (NLC₁) by means of spontaneous parametric down-conversion (SPDC). The signal and idler photons have different central wavelengths, represented in the figure by different colors. The quantum state of the photons generated can be described in the Heisenberg picture by the Bogoliubov transformations [24–26]

$$a_{s_1}(k) = U_{s_1}(k)b_s(k) + V_{s_1}(k)b_i^\dagger(-k), \\ a_{i_1}(k) = U_{i_1}(k)b_i(k) + V_{i_1}(k)b_s^\dagger(-k), \quad (6)$$

where a_{s_1} and a_{i_1} are the signal and idler photon annihilation operators at the output face of the first nonlinear crystal and b_s and b_i are the operators at the input face. See Appendix A for expressions of the functions U_{s_1, i_1} and V_{s_1, i_1} .

The idler photons are reflected from the sample. The idler annihilation operator transforms as

$$a_{i_1}(k) \implies r(k)a_{i_1}(k) + f(k), \quad (7)$$

where the operators $f(k)$ fulfill the commutation relations $[f(k), f^\dagger(k')] = [1 - |r(k)|^2]\delta(k - k')$. These operators take into account the reflection of the idler photons from a sample with reflectivity $r(k)$ [27]. After reflection the idler photons are injected into a second nonlinear crystal (NLC₂), where signal photons s_2 and outgoing idler photons, indistinguishable from the injected idler photons, are generated by means of parametric amplification. Signal photons s_1 and s_2 are combined on a beam splitter and the spectral density $S_2(k)$ of the resulting interference signal is measured. One can show that the spectral density of the output beam is (see Appendix A for details)

$$S_2(k) = |V_{s_2}(k)|^2 [1 - |r(-k)|^2] + |V_{s_1}(k) \exp[ik_s(k)z_1] + r^*(-k)U_{i_1}^*(-k)V_{s_2}(k) \times \exp[-ik_i(-k)z_2 + ik_s(k)z_3]|^2, \quad (8)$$

where $z_{1,2,3}$ are distances that signal and idler photons traverse as indicated in Fig. 1(b). In particular, z_1 is the distance traversed by signal photons s_1 from the output face of NLC₁ to the beam splitter; z_2 is the distance that idler photons i_1 traverse, from the output face of NLC₁ to the sample and from there to the input face of NLC₂; and z_3 is the distance that signal photons s_2 traverse from the output face of NLC₂ to

the beam splitter. We can write $z_3 + z_2 = z_1 + 2s$, so $2s$ is the path imbalance between signal photons s_1 and s_2 that interfere at the beam splitter.

There are two important regimes in parametric down-conversion: the low- and high-parametric-gain regimes. Which regime takes place depends on the value of the nonlinear coefficient [26]

$$\sigma = \left(\frac{\hbar\omega_p\omega_s\omega_i[\chi^{(2)}]^2F_0}{8\epsilon_0c^3Sn_p n_s n_i} \right)^{1/2}, \quad (9)$$

where $F_0 = P_0/\hbar\omega_p$ is the flux rate density of pump photons (photons/s), S is the area of the pump beam, P_0 is the pump power, $\chi^{(2)}$ is the value of the second-order nonlinear susceptibility of the crystal, $\omega_{p,s,i}$ are the central angular frequencies of all waves involved, and $n_{p,s,i}$ are the corresponding refractive indices. The parametric gain is defined as $G = \sigma L$.

At $G \ll 1$, the number of down-converted photons generated per mode is much lower than 1 and the total photon flux is low. Although this can be a drawback of OCT in the low-gain regime, this low photon flux can also be beneficial in applications that require a minimal photodose and where imaging at the video rate can still be achieved [28]. Most implementations of OCT based on nonlinear interferometers are in the low-gain regime [5–7]. In the high-parametric-gain regime $G \gg 1$, the number of photons per mode is higher than one [8,29]. Higher photon fluxes can be achieved in this regime and effects like induced coherence can still be observed [30,31].

In the low-parametric-gain regime ($G \ll 1$), we can write $U_s(k) \sim \exp[ik_s(k)L]$ and $U_i(k) \sim \exp[ik_i(k)L]$. We obtain a simpler expression for the spectrum $S_2(k)$,

$$S_2(k) = |V_{s_1}(k)|^2 \{ 1 + R_1^{1/2} \cos[k(2s + cD_iL) - \varphi_1] + R_2^{1/2} \cos[k(2s + 2n_gd + cD_iL) - \varphi_2] \}, \quad (10)$$

where $\varphi_1 = k_s^0 z_1 + k_i^0 n_i L - k_i^0 z_2 - k_s^0 z_3 + \Delta\varphi_p$, $\varphi_2 = \varphi_1 + 2k_i^0 n_0 d$, and $\Delta\varphi_p = \varphi_{p_1} - \varphi_{p_2}$ is the phase difference between the two pump beams that pump the two nonlinear crystals. They originate from the same laser, but they can bear different phases. Here $k_{s,i}^0$ are central wave numbers at the signal and idler wavelengths, $n_{s,i}$ are the refractive indices inside the nonlinear crystals, and $D_{s,i}$ are the corresponding inverse group velocities.

The Fourier transform of the spectral density $S_2(k)$ in the low-parametric-gain regime is

$$\begin{aligned} \tilde{S}_2(z) = & \tilde{V}_s(z) + \frac{R_1^{1/2}}{2} [\tilde{V}_s(z + 2s + cD_iL) \exp(i\varphi_1) \\ & + \tilde{V}_s(z - 2s - cD_iL) \exp(-i\varphi_1)] \\ & + \frac{R_2^{1/2}}{2} [\tilde{V}_s(z + 2s + 2n_gd + cD_iL) \exp(i\varphi_2) \\ & + \tilde{V}_s(z - 2s - 2n_gd - cD_iL) \exp(-i\varphi_2)], \quad (11) \end{aligned}$$

where $\tilde{V}_s(z)$ is the Fourier transform of $|V_{s_1}(k)|^2$. We define the width of the function $\tilde{V}_s(z)$ as Δz_2 . To observe clear peaks in the output signal \hat{S}_2 , which allows the unequivocal determination of the position of the interfaces of the sample, it is necessary that $2s + cD_iL \gg \Delta z_2$ and $2n_gd \gg \Delta z_2$.

One important difference with the signal in standard OCT [see Eq. (3)] is that the Fourier-transformed spectrum shows only five peaks: one peak at $z = 0$, two peaks for $z > 0$, and two peaks for $z < 0$. The peaks at $z \neq 0$ are located symmetrically around $z = 0$. There are no terms equivalent to the autocorrelation peaks of standard OCT. The distance between the two peaks at $z > 0$ (or $z < 0$) is $2n_gd$, which gives the optical thickness of the sample.

Finally, for the sake of clarity, we caution the following. In [32] an OCT scheme was demonstrated that was termed as quantum OCT (QOCT). QOCT uses paired photons generated in SPDC and quantum interference in a Hong-Ou-Mandel scheme. Therefore, it requires the measurement of second-order correlation functions that translate into the detection of two-photon coincidences [33]. Optical coherence tomography schemes based on nonlinear interferometers are fundamentally different. While they also make use of paired photons generated in SPDC, they do not require the detection of coincidences and are therefore much simpler. A comparison of the advantages and disadvantages of both quantum schemes is an interesting topic but it is outside the scope of our present analysis.

IV. FOURIER-DOMAIN OPTICAL COHERENCE TOMOGRAPHY IN AN SU(1,1) CONFIGURATION

Figure 1(c) shows a sketch of an OCT scheme based on an SU(1,1) interferometer [7,8,17]. Signal (s_1) and idler (i_1) photons generated in the first pass by the nonlinear crystal are separated with the help of a dichroic mirror. Signal photons are reflected and injected back into the same nonlinear crystal. The idler photons are reflected from the sample before traveling back to the nonlinear crystal. After parametric amplification in the second pass of the pump through the nonlinear crystal, the signal photon s_2 is sent to a spectrometer. The spectral density of the signal photons is (see Appendix A for further details)

$$S_3(k) = |V_{s_2}(k)|^2 [1 - |r(-k)|^2] |U_{s_2}(k) V_{s_1}(k) \exp[i\varphi_s(k)] + r^*(-k) U_{i_1}^*(-k) V_{s_2}(k) \exp[-i\varphi_i(-k)]|^2, \quad (12)$$

where $\varphi_s(k) = 2(k_s^0 + k)z_1$ and $\varphi_i(k) = 2(k_i^0 + k)z_2$, with $2z_1$ and $2z_2$ the distances traversed by signal and idler photons before entering the nonlinear crystal.

In the low-parametric-gain regime, the expression for the spectral density simplifies to

$$S_3(k) = 2|V_{s_1}(k)|^2 \{ 1 + R_1^{1/2} \cos[k(2s + cDL) - \varphi_1] + R_2^{1/2} \cos[k(2s + 2n_gd + cDL) - \varphi_2] \}, \quad (13)$$

where the group-velocity mismatch is $D = D_i - D_s$, the path imbalance between signal and idler photons is $2s = 2(z_2 - z_1)$, $\varphi_1 = k_s^0 n_s L + k_i^0 n_i L + 2k_s^0 z_1 + 2k_i^0 z_2 + \Delta\varphi_p$, and $\varphi_2 = \varphi_1 + 2k_i^0 n_0 d$. The Fourier transform of $S_3(k)$ in the low-parametric-gain regime is

$$\begin{aligned} \tilde{S}_3(z) = & 2\tilde{V}_s(z) + R_1^{1/2} [\tilde{V}_s(z + 2s + cDL) \exp(i\varphi_1) \\ & + \tilde{V}_s(z - 2s - cDL) \exp(-i\varphi_1)] \\ & + R_2^{1/2} [\tilde{V}_s(z + 2s + 2n_gd + cDL) \exp(i\varphi_2) \\ & + \tilde{V}_s(z - 2s - 2n_gd - cDL) \exp(-i\varphi_2)], \quad (14) \end{aligned}$$

where $\tilde{V}_s(z)$ is the Fourier transform of $|V_{s_1}(k)|^2$. Again the Fourier-transformed spectrum shows five peaks. The signal for OCT in an SU(1,1) scheme is very similar to the OCT signal for an induced coherence scheme. The main difference is that now, to observe clear peaks in the output signal $\hat{S}_3(z)$, it is necessary that $2s + cDL \gg \Delta z_2$, where $D = D_i - D_s$, in contrast to the case of induced coherence, that is, $2s + cD_iL \gg \Delta z_2$. Since $D_i \ll D$, in an induced coherence scheme the requirement of large path imbalance is not so stringent.

In certain applications, for instance, in biological imaging and in art conservation studies, the power of the light beam that interacts with the sample is low to avoid damage to the sample if too many photons are absorbed. An important advantage of the SU(1,1) configuration in the high-parametric-gain regime, when compared with standard and induced coherence OCT schemes, is that the flux rate of photons that interacts with the sample, $N_{i_1} = \langle a_{i_1}^\dagger(t)a_{i_1}(t) \rangle$, is much lower than the flux rate of photons that are detected, $N_{s_2} = \langle a_{s_2}^\dagger(t)a_{s_2}(t) \rangle$. We define the amplification factor as $\gamma = N_{s_2}/N_{i_1}$. We should note that even though the theoretical analysis in the high-parametric-gain regime considers a cw pump with the corresponding nonlinear coefficient, in experiments one needs to use a pulsed pump with high-energy pulses that are highly focused. Notwithstanding, the approximation of cw and plane-wave pump beams is still valid [25,34].

In Fig. 2 we plot the maximum (red dotted line) and minimum (blue dotted line) values of the amplification factor γ as a function of the reflectivity of a single-layer sample r . The value of the amplification factor depends on the phase difference between the pump beams in the two nonlinear crystals and the phases that the signal and idler photons acquire before seeding the nonlinear parametric amplification process in the second pass by the nonlinear crystal. The maximum of the amplification factor takes place for a global phase difference of 0, while the minimum of the amplification factor takes place for a phase difference of π .

To get further insight, we consider the single-mode description of OCT based on an SU(1,1) interferometer. This is equivalent to considering a single frequency $k = 0$ in the spectral density given by Eq. (12). We obtain that the flux rate of photons interacting with the sample is

$$N_{i_1} = |V|^2 \quad (15)$$

and the flux rate of the signal photons detected is

$$N_{s_2} = |V|^2[(1 - |r|^2) + (1 + |r|^2)|U|^2 + 2|r||U|^2 \cos \theta]. \quad (16)$$

Here $|U| = |U_s(k=0)| = |U_i(k=0)|$, $|V| = |V_s(k=0)| = |V_i(k=0)|$, and θ summarizes the phases that appear in Eq. (12). The maximum and minimum values of the amplification factor in the single-mode approximation are

$$\begin{aligned} \max(\gamma) &= 1 - |r|^2 + (1 + |r|^2)|U|^2, \\ \min(\gamma) &= 1 - |r|^2 + (1 - |r|^2)|U|^2. \end{aligned} \quad (17)$$

These values are also plotted in Fig. 2 as solid lines (red depicts the maximum and blue the minimum value).

For low parametric gain, the approximate (single-mode) and exact values of the amplification factor are barely distinguishable. For high parametric gain we observe that the

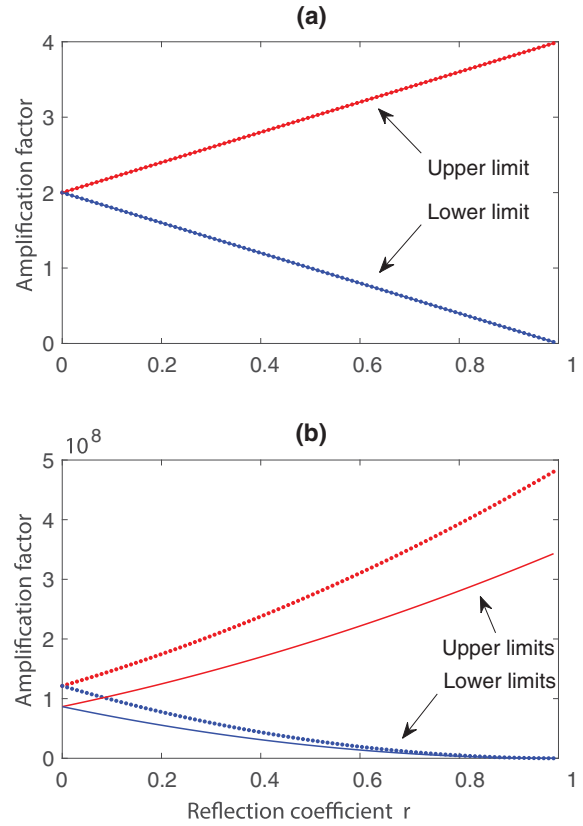


FIG. 2. Amplification factor γ , i.e., the ratio of the signal power at the detection stage and the idler power probing the sample, as a function of the single-interface reflectivity r for two values of the parametric gain G : (a) $G = 0.01$ (low parametric gain) and (b) $G = 10$ (high parametric gain). Dotted lines show the exact solution and solid lines the results obtained using the single-mode approximation. Red lines indicate the maximum value of the amplification factor for a given r and blue lines the minimum value of the amplification factor for a given r .

simple consideration of single-mode parametric amplification provides a very good approximation to the exact values of the amplification factor. For low reflectivity the amplification factor can be approximated as $\gamma = 1 + |U|^2 = 1 + \cosh^2 G$ and does not depend on the phase θ . For high reflectivity the amplification factor can vary between 0 and $\gamma = 4|U|^2 = 4 \cosh^2 G$.

For comparison, in the case of induced coherence the flux rate of photons interacting with the sample is, similarly to the case of an SU(1,1) interferometer, $N_{i_1} = |V|^2$. Now there are two signal beams: The flux rate of signal photons generated in the first nonlinear crystal s_1 is $N_{s_1} = |V|^2$, while the flux rate of signal photons generated in the second nonlinear crystal is $N_{s_2} = |V|^2(1 + |r|^2|V|^2)$.

V. COMPARISON OF THE SIGNALS OBTAINED IN THE THREE OCT CONFIGURATIONS CONSIDERED

Figure 3 shows the spectrum $S_i(k)$ ($i = 1, 2, 3$) and its Fourier transform $|\hat{S}_i(z)|$ for the three cases considered here in the low-parametric-gain regime. Due to the symmetry of the figure, we plot only the signal for $z \geq 0$. In standard OCT we

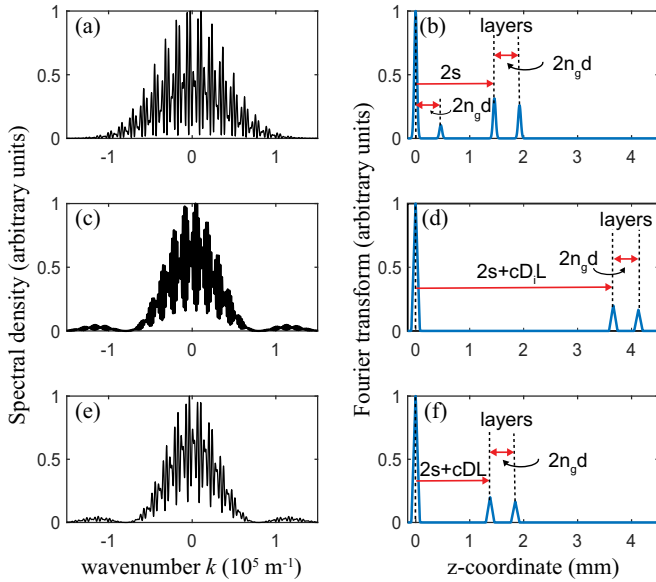


FIG. 3. Spectral density and its Fourier transform in the three OCT schemes considered: (a) and (b) standard OCT, (c) and (d) OCT with induced coherence, and (e) and (f) OCT with an SU(1,1) interferometer. The sample thickness of the bilayer structure considered is $d = 100 \mu\text{m}$, the refractive index n_0 and group index n_g are equal to 2.33, and the path imbalance is $s = 730 \mu\text{m}$. The spectral density and its Fourier transform are depicted in arbitrary units.

consider a light beam with central wavelength $\lambda = 810 \text{ nm}$ and bandwidth $\Delta\lambda = 10 \text{ nm}$. For the quantum schemes, we consider a MgO-doped lithium niobate crystal with length $L = 1 \text{ mm}$ and parameters $cDL = -79.1 \mu\text{m}$ and $cD_iL = 2.2 \text{ mm}$. The wavelength of the signal and idler photons generated in parametric down-conversion are $\lambda_s^0 = 810 \text{ nm}$ and $\lambda_i^0 = 1550 \text{ nm}$, respectively. The wavelength of the pump beam is $\lambda_p = 532 \text{ nm}$. We consider a layer with thickness $d = 100 \mu\text{m}$ and refractive index n_0 and group refractive index n_g equal to 2.33. The optical thickness is thus $n_0d = 233 \mu\text{m}$. We consider reflection coefficients $R_1 = 0.16$ and $R_2 = 0.11$ for the first and second interfaces of the sample, respectively.

The main difference between standard OCT and the two other schemes is that the signal obtained in standard OCT shows peaks corresponding to autocorrelation and cross-correlation terms, while there are no autocorrelation terms in the two other cases. When comparing the OCT signals based on induced coherence and an SU(1,1) interferometer, we observe that the only appreciable difference between them is that the peaks at $z \neq 0$ are farther away from the central peak at $z = 0$ for the case of induced coherence. The reason for this is that the peaks are located at $2s + cDL$ for the SU(1,1) configuration and at $2s + cD_iL$ for the induced coherence configuration.

Equations (3), (8), and (12) are exact expressions that give the spectral density that should be obtained in the three OCT systems considered, for a sample with an arbitrary reflection coefficient $r(k)$. To retrieve the sought-after internal structure of the sample under investigation, one needs to Fourier transform these expressions. Since most experiments take place in the low-parametric-gain regime, we have also derived

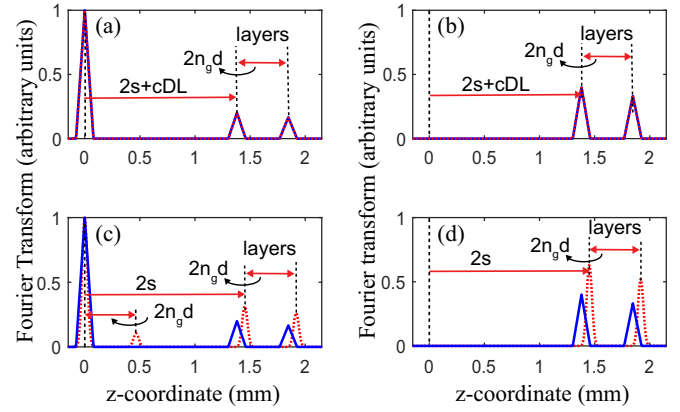


FIG. 4. Fourier transform of the spectral density for OCT based in a SU(1,1) configuration for two values of the parametric gain: (a) and (b) $G = 0.01$ (low parametric gain) and (c) and (d) $G = 10$. Blue solid lines show the analytical approximation valid for the low parametric gain regime given by Eq. (14) for a value of the gain $G = 0.01$. Red dotted lines correspond to the exact expression obtained by Fourier transforming Eq. (12). We consider a nonlinear crystal with the parameters $D_s = 7.61 \times 10^{-9} \text{ s/m}$ and $D_i = 7.34 \times 10^{-9} \text{ s/m}$. We have $cDL = -79.1 \mu\text{m}$ and $cD_iL = 2.2 \text{ mm}$. The reflection coefficients are $R_1 = 0.16$ and $R_2 = 0.11$ for the first and second interfaces of the single-layer sample, respectively. (b) and (d) Result of the subtraction of two measurements are shown with the phases in the reference arm differing by π .

simplified expressions (10) and (13) for the spectral density that should be obtained in this regime. We have done it for the specific benchmark sample we are considering.

The question arises how the shape of the OCT signal expected in the high-parametric-gain regime, given by Eq. (12) in general, compares with the equivalent signal in the low-parametric-gain regime, given by Eq. (14). We consider the case of OCT based on an SU(1,1) scheme, where OCT experiments has been reported in both the low- [6,7] and high-parametric-gain [8] regimes.

Figures 4(a) and 4(c) show the Fourier transform of the expression given by Eq. (12) (red dotted lines) and the analytical approximation of the Fourier transform (blue solid lines) given by Eq. (14) and valid in the low-parametric-gain regime. As expected, both expressions give the same result for a low gain of $G = 0.01$ [Fig. 4(a)]. For large gain $G = 10$ [Fig. 4(c)], we still observe the two peaks corresponding to the two interfaces of the single layer separated a distance $2n_gd$. However, the amplitudes of the peaks of the Fourier transform change and do not have a straightforward relationship with the reflectivity of the layers of the sample as it is the case in the low-parametric-gain regime. Moreover, a new peak at a distance $2n_gd$ appears that can make it difficult, in principle, to resolve the axial structure of the sample. All parametric regimes share the presence of an intense dc component that otherwise bears no relevant information about the sample.

In standard OCT it has been demonstrated [35–37] that one can obtain a signal without the autocorrelation and dc terms by subtracting the spectral densities obtained in two measurements. In one of these measurements, a π phase is introduced into the beam propagating in the reference arm. In OCT based

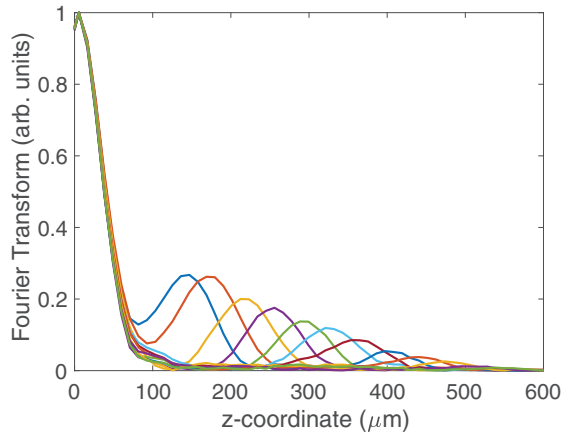


FIG. 5. Sensitivity decay in an OCT scheme based on an SU(1,1) interferometer. The idler photons are reflected from a mirror with ideal reflectivity $r = 1$ located at different axial positions. The spectral density of signal photons is measured for each position and we plot here the Fourier transform of the spectral density, which shows the location of the mirror and its reflectivity. The heights of all peaks would be the same for ideal pointlike pixels. However, the finite size of the pixels at the detection stage causes an apparent decay of the value of the reflectivity. Experimental data were obtained from [8]. Different colors correspond to different positions of the mirror.

on nonlinear interferometers, the dc term is still present. We apply this procedure to the signals $S_3(k)$ shown in Figs. 4(a) and 4(c). In our case we need to subtract two spectral densities given by Eq. (12) with phases $\varphi_s(k)$ and $\varphi_s(k) + \pi$ and from Eq. (13) with phases $\varphi_1(k)$ and $\varphi_1(k) + \pi$. Figures 4(b) and 4(d) show the results. The central peak is removed as expected. However, also the new peak that appears for $G = 10$ is removed, so in this respect this peak behaves similarly to the self-correlation term in standard OCT.

One important result of the present work is that all OCT schemes might share similar technological limitations. For instance, it is well known that the finite size of pixels in spectrometers in general and in high-sensitivity CCD cameras in particular leads to a sensitivity decay as a function of path imbalance [38–41]. This sensitivity decay needs to be corrected to obtain high-resolution and accurate images of samples. Figure 5 shows an example of this sensitivity decay for an OCT scheme based on an SU(1,1) interferometer with gain $G = 1.7$. These experimental data are obtained from [8]. This is an example that shows that the experience obtained in research associated with standard OCT schemes can be beneficial also for new OCT schemes based on nonlinear interferometers.

VI. CONCLUSION

We have analyzed the signal of interest in three different OCT schemes. The characteristics of the signal enable the optical sectioning of samples in axial scans. For the sake of comparison, we considered standard OCT and two other schemes that make use of nonlinear interferometers. One is based on the concept of induced coherence and the other on an SU(1, 1) interferometer. We have considered Fourier-domain OCT, where the axial internal structure of the sample is

obtained from the Fourier transform of the signal. Our analysis provides an overview of tomographic images acquired with OCT schemes that make use of nonlinear interferometers.

The signal in standard OCT shows both unwanted autocorrelation terms and cross-correlation terms, which carry the sought-after information about the sample. A distinguishing characteristic of OCT schemes based on nonlinear interferometers in the low-parametric-gain regime is that they do not show any autocorrelation terms. However, there are techniques that make use of the phases that accompany each term to remove self-reference terms and even the peak at $z = 0$ [35–37]. When considering these techniques, which have been successfully demonstrated in several OCT schemes, the signal obtained in the three OCT schemes turns out to be essentially the same for the representative sample consider here. We expect a similar behavior for other types of samples.

The only difference remaining is in the location of peaks of interest at $z \neq 0$. For our benchmark example, in the low-parametric-gain regime, the peaks at $z > 0$ corresponding to the first interface, after Fourier transform, are located at $2s$, $2s + cD_iL$, and $2s + cDL$ for the three OCT schemes considered, respectively. This was clearly seen in Fig. 3. This puts different conditions on the path imbalance s required to obtain a clear image of the internal structure of the sample in Fourier-domain OCT.

Optical coherence tomography based on nonlinear interferometers has the advantage that the sample can be probed at one wavelength, while detection occurs at another wavelength. Both wavelengths can be chosen independently to optimize probing and detection.

ACKNOWLEDGMENTS

This work is part of the RD Project No. CEX2019-000910-S, funded by Grant No. MCIN/AEI/10.13039/501100011033. It is supported by Fundació Cellex, Fundació Mir-Puig, and Generalitat de Catalunya through the CERCA program. We acknowledge financial support from project QUISPAMOL (Project No. PID2020-112670GB-I00) funded by Grant No. MCIN/AEI/10.13039/501100011033. This work was also part of the Project No. 20FUN02 “PO-Light,” which received funding from the EMPIR program cofinanced by the Participating States and from the European Union’s Horizon 2020 research and innovation program. D.L.-M. acknowledges funding from Consejo Nacional de Ciencia y Tecnología (Grants No. 293471, No. 295239, and No. APN2016-3140). A.R.-S. acknowledges support from Becas de Movilidad CONACYT. G.J.M. was supported by the Secretaria d’Universitats i Recerca del Departament d’Empresa i Coneixement de la Generalitat de Catalunya and European Social Fund.

APPENDIX A: QUANTUM STATE OF PAIRED PHOTONS GENERATED IN PARAMETRIC DOWN-CONVERSION

1. Input-output relationships in parametric down-conversion

A nonlinear crystal (length L) is pumped by an intense cw laser beam with wavelength λ_p . The wave number of the pump beam is $k_p = 2\pi n_p/\lambda_p$, with n_p the refractive index at λ_p . The interaction of the pump beam with the crystal mediates the

generation of pairs of correlated photons (signal and idler) by means of spontaneous parametric down-conversion. The paired photons generated are frequency anticorrelated, i.e., $k_s = k_s^0 + k$ and $k_i = k_i^0 - k$, where $k_{s,i}$ are the wave numbers of signal or idler photons, $k_{s,i}^0$ are the corresponding central wave numbers, and $\pm k$ is the wave-number deviation from the corresponding central wave number.

We assume that the bandwidth of the photons is much larger than the bandwidth of the pump beam. We also assume that the Rayleigh length ($L_R = k_p^0 w_p^2/2$) of the pump beam is much larger than the crystal length. Here w_p is the pump beam waist and $k_p^0 = 2\pi n_p/\lambda_p^0$ is the pump beam wave number. Under these conditions we can describe the spatiotemporal characteristics of parametric down-conversion using the cw and plane-wave pump beam approximations. The Bogoliubov transformations that relate the quantum operators for signal and idler photons (a_s and a_i) at the output face of the nonlinear crystal to the quantum operators at the input face of the nonlinear crystal (b_s and b_i) are [24–26]

$$\begin{aligned} a_s(k) &= U_s(k)b_s(k) + V_s(k)b_i^\dagger(-k), \\ a_i(k) &= U_i(k)b_i(k) + V_i(k)b_s^\dagger(-k), \end{aligned} \quad (\text{A1})$$

where

$$\begin{aligned} U_{s,i}(k) &= \left(\cosh(\Gamma_{s,i}L) - i \frac{\Delta_{s,i}}{2\Gamma_{s,i}} \sinh(\Gamma_{s,i}L) \right) \\ &\quad \times \exp\left(i\delta_{s,i} \frac{L}{2}\right), \\ V_{s,i}(k) &= -i \frac{\sigma}{\Gamma_{s,i}} \sinh(\Gamma_{s,i}L) \exp\left(i\delta_{s,i} \frac{L}{2} + i\varphi_p\right), \end{aligned} \quad (\text{A2})$$

with $\delta_{s,i} = k_p + k_{s,i}(k) - k_{i,s}(-k)$ and φ_p the phase of the pump beam. The signal and idler beams fulfill the paraxial approximation, so we can expand the corresponding wave numbers in a Taylor series as $k_{s,i} = k_{s,i}^0 + cD_{s,i}k$, where $D_{s,i}$ are inverse group velocities. We assume phase matching at the central frequencies, i.e., $k_p = k_s^0 + k_i^0 \pm 2\pi/\Lambda$, where Λ is the poling period of the nonlinear crystal. The phase-matching function is thus $\Delta_s = -\Delta_i = cDLk$, with $D = D_i - D_s$. The nonlinear coefficient σ is

$$\sigma = \left(\frac{\hbar\omega_p\omega_s\omega_i[\chi^{(2)}]^2 F_0}{8\epsilon_0 c^3 S n_p n_s n_i} \right)^{1/2} \quad (\text{A3})$$

and

$$\Gamma_{s,i} = \left(\sigma^2 - \frac{\Delta_{s,i}^2}{4} \right)^{1/2}. \quad (\text{A4})$$

Here $F_0 = P_0/\hbar\omega_p$ is the flux rate density of pump photons (photons/s), S is the area of the pump beam, and P_0 is the pump power.

The parametric gain is defined as $G = \sigma L$. It provides a measure of the number of photons per mode generated in a parametric down-conversion (PDC) process. Depending on the value of the gain G , the PDC process is said to be in the low-parametric-gain regime if $G \ll 1$, i.e., the number of photons generated per mode is much smaller than one. On the other hand, if the number of photons per mode generated is greater than one, the PDC process is said to be in the high-parametric-gain regime ($G > 1$).

2. Spectrum of signal photons in optical coherence tomography

In an induced coherence scheme, the signal photon annihilation operator at the output facet of the second nonlinear crystal $a_{s_2}(k)$ reads

$$\begin{aligned} a_{s_2}(k) &= U_{s_2}(k)c_s(k) + V_{s_2}(k)a_{i_1}^\dagger(-k) \\ &= U_{s_2}(k)c_s(k) + r^*(-k)V_{s_2}(k)U_{i_1}^*(-k)b_i^\dagger(-k) \\ &\quad + r^*(-k)V_{s_2}(k)V_{i_1}^*(-k)b_s(k) + V_{s_2}(k)f_i^\dagger(-k). \end{aligned} \quad (\text{A5})$$

The signal photons spectrum is $S_2(k) = \langle a_{s_2}^\dagger(k)a_{s_2}(k) \rangle$. Substituting Eq. (A5) into this expression, we obtain the spectrum given in Eq. (8).

In an SU(1,1) nonlinear interferometer, the signal photon annihilation operator at the output facet of the second nonlinear crystal $a_{s_2}(k)$ reads

$$\begin{aligned} a_{s_2}(k) &= U_s(k)a_{s_1}(k) + V_s(k)a_{i_1}^\dagger(-k) \\ &= [U_{s_1}(k)U_{s_2}(k) + r^*(-k)V_{s_2}(k)V_{i_1}^*(-k)]b_s(k) \\ &\quad + V_{s_2}(k)[U_{s_2}(k) + r^*(-k)U_{i_2}^*(-k)]b_i^\dagger(k) \\ &\quad + V_{s_2}(k)f_i^\dagger(-k). \end{aligned} \quad (\text{A6})$$

The signal photons spectrum is $S_3(k) = \langle a_{s_2}^\dagger(k)a_{s_2}(k) \rangle$. Substituting Eq. (A6) into this expression, we obtain the spectrum given in Eq. (12).

APPENDIX B: DESCRIPTION OF THE EFFECT ON THE QUANTUM STATE OF IDLER PHOTONS OF REFLECTION FROM A SAMPLE WITH FREQUENCY-DEPENDENT REFLECTIVITY

The idler beam interacts with a sample with reflectivity $r(k)$. The operator that describes the quantum state of idler photons after reflection from the sample is [27]

$$a_i(k) \implies r(k)a_i(k) + f(k), \quad (\text{B1})$$

where $f(k)$ fulfills the commutation relationship

$$[f(k), f^\dagger(k')] = [1 - |r(k)|^2]\delta(k - k'). \quad (\text{B2})$$

The operator $f(k)$ takes into account the frequency-dependent losses and reflectivity of the sample.

One can obtain in a straightforward way Eqs. (B1) and (B2) considering an ideal situation when idler photons impinge on a beam splitter (BS) with transmissivity $t(k)$ and reflectivity $r(k)$. The BS aims at simulating in a very simple way reflection from the sample. Idler photons enter the BS through input port 1 and we are interested in idler photons reflected from the BS through output port 3. The operator that describes the quantum states of photons in output port 3 is $a_3(k) = r(k)a_1(k) + t(k)a_2(k)$. If we define $f(k) \equiv t(k)a_2(k)$ we obtain Eq. (B1). Moreover, we can write

$$\begin{aligned} [f(k), f^\dagger(k')] &= [t(k)a_2(k), t^*(k')a_2^\dagger(k')] \\ &= |t(k)|^2\delta(k - k') \\ &= (1 - |r(k)|^2)\delta(k - k'), \end{aligned} \quad (\text{B3})$$

that is, Eq. (B2). We have made use of the relationship $|r(k)|^2 + |t(k)|^2 = 1$.

- [1] W. Drexler and J. G. Fujimoto, *Optical Coherence Tomography: Technology and Applications* (Springer Science+Business Media, New York, 2008).
- [2] www.octnews.org.
- [3] D. Huang, E. Swanson, C. Lin, J. Schuman, W. Stinson, W. Chang, M. Hee, T. Flotte, K. Gregory, C. Puliafito, and J. G. Fujimoto, Optical coherence tomography, *Science* **254**, 1178 (1991).
- [4] T. Dresel, G. Hausler, and H. Venzke, Three-dimensional sensing of rough surfaces by coherence radar, *Appl. Opt.* **31**, 919 (1992).
- [5] A. Vallés, G. Jiménez, L. J. Salazar-Serrano, and J. P. Torres, Optical sectioning in induced coherence tomography with frequency-entangled photons, *Phys. Rev. A* **97**, 023824 (2018).
- [6] A. V. Paterova, H. Yang, A. Chengwu, D. A. Kalashnikov, and L. A. Krivitsky, Tunable optical coherence tomography in the infrared range using visible photons, *Quantum Sci. Technol.* **3**, 025008 (2018).
- [7] A. Vanselow, P. Kaufmann, I. Zorin, B. Heise, H. M. Chrzanowski, and S. Ramelow, Frequency-domain optical coherence tomography with undetected mid-infrared photons, *Optica* **7**, 1729 (2020).
- [8] G. J. Machado, G. Frascella, J. P. Torres, and M. V. Chekhova, Optical coherence tomography with a nonlinear interferometer in the high parametric gain regime, *Appl. Phys. Lett.* **117**, 094002 (2020).
- [9] M. V. Chekhova and Z. Y. Ou, Nonlinear interferometers in quantum optics, *Adv. Opt. Photon.* **8**, 104 (2016).
- [10] G. B. Lemos, V. Borish, G. D. Cole, S. Ramelow, R. Lapkiewicz, and A. Zeilinger, Quantum imaging with undetected photons, *Nature (London)* **512**, 409 (2014).
- [11] A. C. Cardoso, L. P. Berruezo, D. F. Ávila, G. B. Lemos, W. M. Pimenta, C. H. Monken, P. L. Saldanha, and S. Pádua, Classical imaging with undetected light, *Phys. Rev. A* **97**, 033827 (2018).
- [12] M. Kutas, B. Haase, P. Bickert, F. Rieinger, D. Molter, and G. von Freymann, Terahertz quantum sensing, *Sci. Adv.* **6**, eaaz8065 (2020).
- [13] D. A. Kalashnikov, A. V. Paterova, S. P. Kulik, and L. A. Krivitsky, Infrared spectroscopy with visible light, *Nat. Photon.* **10**, 98 (2016).
- [14] V. Paterova, H. Yang, D. Kalashnikov, and L. Krivitsky, Measurement of infrared optical constants with visible photons, *New J. Phys.* **20**, 043015 (2018).
- [15] C. Lindner, S. Wolf, J. Kiessling, and F. Kühnemann, Fourier transform infrared spectroscopy with visible light, *Opt. Express* **28**, 4426 (2020).
- [16] I. Kviatkovsky, H. M. Chrzanowski, E. G. Avery, H. Bartolomaeus, and S. Ramelow, Microscopy with undetected photons in the mid-infrared, *Sci. Adv.* **6**, eabd0264 (2020).
- [17] A. V. Paterova, S. M. Maniam, H. Yang, G. Grenci, and L. A. Krivitsky, Hyperspectral infrared microscopy with visible light, *Sci. Adv.* **6**, eabd0460 (2020).
- [18] X. Y. Zou, L. J. Wang, and L. Mandel, Induced Coherence and Indistinguishability in Optical Interference, *Phys. Rev. Lett.* **67**, 318 (1991).
- [19] L. J. Wang, X. Y. Zou, and L. Mandel, Induced coherence without induced emission, *Phys. Rev. A* **44**, 4614 (1991).
- [20] X. Y. Zou, T. P. Grayson, and L. Mandel, Observation of Quantum Interference Effects in the Frequency Domain, *Phys. Rev. Lett.* **69**, 3041 (1992).
- [21] B. Yurke, S. L. McCall, and J. R. Klauder, SU(2) and SU(1,1) interferometers, *Phys. Rev. A* **33**, 4033 (1986).
- [22] A. F. Fercher, C. K. Hitzenberger, G. Kamp, and S. Y. El-Zaiat, Measurement of intraocular distances by backscattering spectral interferometry, *Opt. Commun.* **117**, 43 (1995).
- [23] M. Choma, M. V. Sarunic, C. Yang, and J. A. Izatt, Sensitivity advantage of swept source and fourier domain optical coherence tomography, *Opt. Express* **11**, 2183 (2003).
- [24] A. Gatti, R. Zambrini, M. San Miguel, and L. A. Lugiato, Multiphoton multimode polarization entanglement in parametric down-conversion, *Phys. Rev. A* **68**, 053807 (2003).
- [25] B. Dayan, Theory of two-photon interactions with broadband down-converted light and entangled photons, *Phys. Rev. A* **76**, 043813 (2007).
- [26] J. P. Torres, K. Banaszek, and I. A. Walmsley, Engineering nonlinear optic sources of photonic entanglement, *Prog. Opt.* **56**, 227 (2011).
- [27] R. W. Boyd, G. S. Agarwal, K. W. C. Chan, A. K. Jha, and M. N. O'Sullivan, Propagation of quantum states of light through absorbing and amplifying media, *Opt. Commun.* **281**, 3732 (2008).
- [28] M. Gilaberte Basset, A. Hochrainer, S. Töpfer, F. Rieinger, P. Bickert, J. R. León-Torres, F. Steinlechner, and M. Gräfe, Video-rate imaging with undetected photons, *Laser Photon. Rev.* **15**, 2000327 (2021).
- [29] J. Le Gouët, D. Venkatraman, F. N. C. Wong, and J. H. Shapiro, Classical low-coherence interferometry based on broadband parametric fluorescence and amplification, *Opt. Express* **17**, 17874 (2009).
- [30] A. V. Belinsky and D. N. Klyshko, Interference of classical and non-classical light, *Phys. Lett. A* **166**, 303 (1992).
- [31] H. M. Wiseman and K. Mølmer, Induced coherence with and without induced emission, *Phys. Lett. A* **270**, 245 (2000).
- [32] M. B. Nasr, B. E. A. Saleh, A. V. Sergienko, and M. C. Teich, Demonstration of Dispersion-Canceled Quantum-Optical Coherence Tomography, *Phys. Rev. Lett.* **91**, 083601 (2003).
- [33] P. Y. Graciano, A. M. Angulo Martínez, D. Lopez-Mago, G. Castro-Olvera, M. Rosete-Aguilar, J. Garduño-Mejía, R. Ramírez Alarcón, H. Cruz Ramírez, and A. B. U'Ren, Interference effects in quantum-optical coherence tomography using spectrally engineered photon pairs, *Sci. Rep.* **9**, 8954 (2019).
- [34] K. Y. Spasibko, T. S. Iskhakov, and M. V. Chekhova, Spectral properties of high-gain parametric down-conversion, *Opt. Express* **20**, 7507 (2012).
- [35] M. Wojtkowski, R. Leitgeb, A. Kowalczyk, T. Bajraszewski, and A. F. Fercher, In vivo human retinal imaging by fourier domain optical coherence tomography, *J. Biomed. Opt.* **7**, 457 (2002).
- [36] M. A. Choma, C. Yang, and J. A. Izatt, Instantaneous quadrature low-coherence interferometry with 3×3 fiber-optic couplers, *Opt. Lett.* **28**, 2162 (2003).
- [37] R. A. Leitgeb, C. K. Hitzenberger, A. F. Fercher, and T. Bajraszewski, Phase-shifting algorithm to achieve high-speed long-depth-range probing by frequency-domain optical coherence tomography, *Opt. Lett.* **28**, 2201 (2003).
- [38] R. Leitgeb, C. K. Hitzenberger, and A. F. Fercher, Performance of Fourier domain vs. time domain optical coherence tomography, *Opt. Express* **11**, 889 (2003).
- [39] S. H. Yun, G. J. Tearney, B. E. Bouma, B. H. Park, and J. F. de Boer, High-speed spectral-domain optical coherence

- tomography at $1.3\ \mu\text{m}$ wavelength, [Opt. Express **11**, 3598 \(2003\)](#).
- [40] N. A. Nassif, B. Cense, B. H. Park, M. C. Pierce, S. H. Yun, B. E. Bouma, G. J. Tearney, T. C. Chen, and J. F. de Boer, *In vivo* high-resolution video-rate spectral-domain optical coherence tomography of the human retina and optic nerve, [Opt. Express **12**, 367 \(2004\)](#).
- [41] Z. Hu, Y. Pan, and A. M. Rollins, Analytical model of spectrometer-based two-beam spectral interferometry, [Appl. Opt. **46**, 8499 \(2007\)](#).